Spatial Gradient Monitor for GBAS

Jaymin Patel
Illinois Institute of Technology
Chicago, USA
jpatel97@hawk.iit.edu

Samer Khanafseh
Illinois Institute of Technology
Chicago, USA
khansam1@iit.edu

Boris Pervan
Illinois Institute of Technology
Chicago, USA
pervan@iit.edu

***Abstract*—In this paper, we develop a ground monitor capable of detecting anomalous signal-in-space(SIS) spatial gradients for rising, newly acquired, and re-acquired satellites in the Ground Based Augmentation System (GBAS). These gradients can be caused by satellite orbit ephemeris faults and ionospheric fronts. The monitor utilizes differential code and carrier phase measurement across multiple reference receiver antennas as the basis for detection. We show that the new monitor significantly improves the detection performance over existing fault detection algorithms under tropospheric turbulence and that it is capable of meeting Category III precision approach and landing requirements.**

***Index Terms*—Ionospheric gradient, Orbit ephemeris faults, Initialization of spatial monitor, Tropospheric Turbulence**

I. Introduction

GBAS is a safety-critical navigation system intended to support all phases of approach, landing, departure, and surface operations at an airport. It will include multiple spatially separated Global Positioning System (GPS) antennas and receivers at each Ground Facility (GF). The primary reasons for the use of this redundant hardware are to provide a means for detection and isolation of a failed receiver and also to allow for a net reduction in ranging error by averaging measurements for a given satellite. However, another benefit of antenna separation is that differential carrier phase measurements across the antenna baselines can be used to detect and isolate certain SIS anomalies that are hazardous to GBAS.

There are three types of orbit ephemeris failures [6]: Type B failures occur when the broadcast ephemeris data is incorrect but no satellite maneuver is involved; Type A1 failures occur when the broadcast ephemeris data has been updated incorrectly following a satellite maneuver; Type A2 failure exists if the broadcast ephemeris remains unchanged after the maneuver. Type B failures can be detected by comparing the current ephemeris with a previously validated broadcast ephemeris [7]. In contrast, previous ephemerides provide no benefit for the detection of type A1 and type A2 faults due to the presence of the satellite maneuver. In order to detect these faults, ground monitors based on the range and range rate of the satellite are utilized [6].

Large ionospheric gradients caused by ionospheric storms are significant potential hazards for GBAS [8]. Aircraft on Category III precision approach supported by GBAS Approach Service Type D cannot tolerate ionospheric gradients larger than 300 mm/km in the direction of the runway [9]. However, gradients as large as 412 mm/km have been observed in CONUS, which can cause up to 20 m of vertical positioning error for GBAS users [8].

There has been prior work utilizing multi-antenna code and carrier phase measurements to detect gradient faults [1]–[6]. Most recently, a ground monitor with runway-parallel antenna baselines was developed to satisfy Category III integrity requirements for all types of orbit ephemeris faults [19]. However, this monitor, while sensitive to spatial gradients, was also overly sensitive to other nonthreatening measurement errors. Specifically, short duration localized neutral atmospheric disturbances (sometimes called tropospheric turbulence) can also appear as gradients [21]. This type of tropospheric activity typically exists in the lower atmosphere, and the associated structures have small physical scales relative to ionospheric fronts. They produce much smaller differential measurement errors than ionospheric fronts and are not hazardous to GBAS users. But a major problem remains: they can significantly elevate probability of monitor false alarms. One easy solution would be to loosen the monitor's detection thresholds; we show, unfortunately, that this approach degrades the monitor's detection performance to the point that it would no longer be effective for the Category III application [21]. Another alternative is to attempt to somehow distinguish hazardous ionospheric faults from benign tropospheric turbulence. This was done to some extent in [13], but the solution worked only for certain speed and tropospheric error parameters.

Section II of this paper develops the differential carrier phase monitor that enables the detection of spatial gradients caused by orbit ephemeris faults and ionospheric gradient. Section III shows how to resolve the carrier phase integer ambiguities needed to initialize the monitor. Section IV shows the effect of the cycle resolution process on the monitor's false alarm and missed detection probabilities. Section V describes GBAS performance requirements on ephemeris monitor and Ionospheric Gradient Monitor (IGM). Section VI and VII show the performance of the monitor using single and multiple baselines respectively. In section VIII, we discuss the impact of tropospheric turbulence on the monitor's performance and propose a method to mitigate its effect.

II. Monitor Concept

A. Ephemeris Monitor

Given that the likelihood of two or more simultaneous ephemeris faults is much smaller than the integrity risk requirement, GBAS presumes that only one satellite is affected

by an ephemeris fault at any given time. For a faulty satellite i and a fault-free satellite j, the differential carrier phase measurement for antenna 1 is

$$\begin{aligned}\Delta\phi_1 &= (r_1^i - r_1^j + \Delta I + \Delta T + \delta t_s) + \lambda\Delta n_1 + \Delta\nu_{\phi_1} \\ &= \tilde{r} + \lambda\Delta n_1 + \Delta\nu_{\phi_1}\end{aligned} \tag{1}$$

where r_1^i and r_1^j are the ranges between antenna 1 and satellite i and j, respectively, ΔI is the single difference ionospheric error, ΔT is the single difference tropospheric error, δt_s is the single difference satellite clock bias, λ is the carrier wavelength, Δn_1 is the single difference cycle ambiguity for antenna 1 and $\Delta\nu_{\phi_1}$ is the single difference measurement error for antenna 1.

Similarly, the differential carrier phase measurement for antenna 2 can be written as

$$\begin{aligned}\Delta\phi_2 &= (r_2^i - r_2^j + \Delta I + \Delta T + \delta t_s) + \lambda\Delta n_2 + \Delta\nu_{\phi_2} \\ &= \tilde{r} + (r_2^i - r_1^i) - (r_2^j - r_1^j) + \lambda\Delta n_2 + \Delta\nu_{\phi_2}\end{aligned} \tag{2}$$

The differential range between the two antennas $(r_2^i - r_1^i)$ is equal to the dot product of the true differential line of sight unit vector from antenna 1 to satellite i $(e_{i,true}^T)$ and the baseline position vector between the two antennas (b_{12}). Because satellite i is assumed to be faulty, the line of sight unit vector computed from the ephemeris $(e_{i,true}^T)$ is faulted. Therefore,

$$r_2^i - r_1^i = e_{i,true}^T b_{12} = (e_{i,eph}^T + \delta e_i^T) b_{12} \tag{3}$$

where δe_i^T is the 3×1 ephemeris fault vector and b_{12} is the 3×1 relative position vector between antennas 1 and 2 expressed in the local North-East-Down (NED) frame.

Since satellite j is assumed to be fault free, the true line of sight unit vector between antenna 1 and satellite j is equivalent to the vector computed from the ephemeris,i.e.,

$$r_2^j - r_1^j = e_{j,true}^T b_{12} = e_{j,eph}^T \tag{4}$$

By substituting equations (3) and (4) into equation (2), the measurement received by antenna 2 can be expressed as

$$\begin{aligned}\Delta\phi_2 &= \tilde{r} + e_{i,eph}^T b_{12} + \delta e_i^T b_{12} - e_{j,eph}^T b_{12} + \lambda\Delta n_2 + \Delta\nu_{\phi_2} \\ &= \tilde{r} + \Delta e^T b_{12} + b_{12}^T \delta e_i + \lambda\Delta n_2 + \Delta\nu_{\phi_2}\end{aligned} \tag{5}$$

where $\Delta e^T = e_{i,eph}^T - e_{j,eph}^T$.

Taking the difference between two antennas (to form the double difference),

$$\begin{aligned}\Delta^2\phi_{12} &= \Delta\phi_2 - \Delta\phi_1 \\ &= \Delta e^T b_{12} + b_{12}^T \delta e_i + \lambda(\Delta n_2 - \Delta n_1) + \Delta^2\nu_{\phi_{12}}\end{aligned} \tag{6}$$

where $\Delta\nu_{\phi_{12}}$ is the double difference carrier phase measurement error.

Assuming that ambiguities are known, which will be discussed in the following section, the test statistic can be formed as,

$$q = \Delta_{\phi_{12}}^2 - \Delta e^T b_{12} - \lambda(\Delta n_2 - \Delta n_1) = b_{12}^T \delta e_i + \Delta^2\nu_{\phi_{12}} \tag{7}$$

Under fault-free conditions, the test statistic is normally distributed with a zero mean and standard deviation as the double difference carrier phase measurement noise $\sigma_{\Delta^2\phi}$. Due to the low noise in the carrier phase measurements, the test statistic in (7) will be sensitive to Ephemeris faults, as we will show later.

B. Ionospheric Gradient Monitor (IGM)

In [14], a monitor utilizing differential carrier phase measurements across multiple reference stations was introduced to instantaneously detect ionospheric gradients. The simplified double difference carrier phase measurement model between two antennas for a faulted satellite i and a fault-free satellite j is given by

$$\Delta^2\phi_{12} = \Delta e^T b_{12} + \lambda\Delta^2 n_{12} + \Delta I + \Delta^2\nu_{\phi_{12}} \tag{8}$$

where $\Delta^2\phi_{12}$ is double difference carrier phase measurement. Δe is the differential user-satellite line of sight unit vector. $\Delta^2 n$ is double difference cycle ambiguity, and ΔI is differential ionospheric error between antennas.

The ionospheric anomaly ΔI is described by the following model [15]

$$\Delta I = b_{12}^T \alpha \tag{9}$$

Therefore, the test statistics can be formed, assuming known ambiguities as we will show in the next section, as

$$q = \Delta^2\phi_{12} - \Delta e^T b_{12} - \lambda\Delta^2 n_{12} = b_{12}^T\alpha + \Delta^2\nu_{\phi_{12}} \tag{10}$$

Comparing equation (7) and (10), we can see that the monitor is quite similar and that its test statistics sensitivity is directly influenced by the baseline length.

III. Monitor Initialization

A. Resolving the cycle ambiguity for the Ephemeris Monitor

The cycle ambiguity estimate required to compute q in in (7) needs to be immune to the ephemeris fault. We may eliminate the dependency on the ephemeris by differencing the pseudorange measurements from the carrier phase:

$$Z_{CMC} = \phi - \rho = \lambda n - 2I + \nu_\phi - \nu_\rho \tag{11}$$

The effect of ionospheric errors can be attenuated by taking the difference of Z_{CMC} between two antennas (12).

$$\Delta Z_{CMC_{12}} = Z_{CMC_2} - Z_{CMC_2} = \lambda\Delta n - 2\Delta I + \Delta\nu_\phi - \Delta\nu_\rho \tag{12}$$

The error in $\Delta Z_{CMC_{12}}$ is dominated by thermal noise and multipath errors in $\Delta\nu_\rho$, which are much larger than the sub-cm level carrier phase noise or the 2-4 mm/km differential ionospheric residual errors (vertical errors). Filtering ΔZ_{CMC12} reduces the effect of these errors and may allow resolving the integer ambiguity term Δn_{12} (13).

$$\Delta\hat{n}_{12} = \frac{\sum \Delta Z_{CMC_{12}}}{\tau} = \Delta n_{12} + \varepsilon_{\Delta\hat{n}} \tag{13}$$

where τ is the estimated number of independent samples being averaged and

$$\varepsilon_{\Delta\hat{n}} \sim N(0, \frac{\sigma_{Z_{CMC}}}{\sqrt{\tau}}) \tag{14}$$

B. Resolving the cycle ambiguity for IGM

Similarly, we will use the pseudorange measurement to estimate the cycle ambiguities, by adding it to carrier phase measurement, to eliminate the effect of the ionospheric fault:

$$\phi + \rho = 2(r + T + c(\delta t^{sat} - \delta t_{rec})) + \lambda n + \nu_\phi + \nu_\rho \quad (15)$$

The effect of nominal tropospheric delay and clock bias errors can be attenuated by taking the double difference of $\phi + \rho$ between two satellites and two antennas (16). Since this monitor operates under fault-free ephemeris hypothesis, the range term $\Delta^2 r$ is known and can be evaluated as $\Delta e^T b_{12}$, which leads to, equation (17)

$$\Delta^2(\phi + \rho) = 2\Delta^2 r + \lambda\Delta^2 n + \Delta^2\nu_\phi + \Delta^2\nu_\rho \quad (16)$$

$$\Delta^2 Z_{CPC} = \Delta^2(\phi + \rho) - 2\Delta e^T b_{12} = \lambda\Delta^2 n + \Delta^2\nu_\phi + \Delta^2\nu_\rho \quad (17)$$

The error in $\Delta^2 Z_{CPC}$ is dominated by thermal noise and multipath errors in $\Delta^2\nu_\rho$. Filtering $\Delta^2 Z_{CPC}$ reduces the effect of these errors and may allow resolving the integer ambiguity term $\Delta^2 n$ (18).

$$\Delta^2\hat{n} = \frac{\sum \Delta^2 Z_{CPC}}{\tau} = \Delta^2 n + \varepsilon_{\Delta^2\hat{n}} \quad (18)$$

where τ is the estimated number of independent samples being averaged and

$$\varepsilon_{\Delta^2\hat{n}} \sim N(0, \frac{\sigma_{Z^2_{CPC}}}{\sqrt{\tau}}) \quad (19)$$

C. Impact of the rounding process on the test statistics

The float ambiguity estimate in (13) and (18) may not be sufficient to meet the requirements. The error in the float ambiguity estimate itself must be incorporated to the test statistic q in (7) and (10). One way to reduce the estimate error is by increasing the filtering period. But to reach the level of the carrier phase noise in q, and thus have minimal impact on the monitor's detection capabilities, filtering periods lasting hours would be necessary. Therefore, this approach is deemed not practical.

Instead, the integer ambiguity can be computed by rounding the averaged value of $\Delta\hat{n}$ and $\Delta^2\hat{n}$. The introduction of rounding means that the test statistic error will be the same as the carrier phase noise error (no impact). However, the rounding process, which is nonlinear and may result in correct or incorrect integers, will cause the test statistic to be mixed Gaussian distribution (Figure 1). Therefore, the likelihood of rounding to the wrong ambiguity must be accounted for. Recall that since ΔZ_{CMC} and $\Delta^2 Z_{CPC}$ are fault free, only noise may cause the ambiguity to be rounded to the wrong integer. Under fault-free conditions, a wrong ambiguity fix will cause the test statistic to be biased, which may cause a false alarm. Under the fault hypothesis, this incorrect fix may mask the actual fault, and thus causing a missed detection.

The probability of rounding to the correct ambiguity, or any specific incorrect one, can be computed from the Gaussian cumulative distribution function (CDF) given the distribution of $\varepsilon_{\Delta\hat{n}}$ and $\varepsilon_{\Delta^2\hat{n}}$ in (14) and (19) respectively. For example,

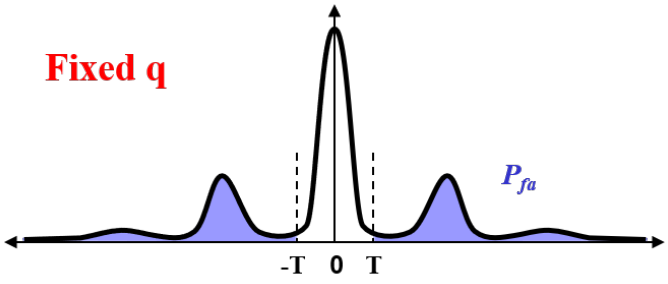

Fig. 1. Illustration of the mixed Gaussian distribution of the test statistic q as a result of rounding

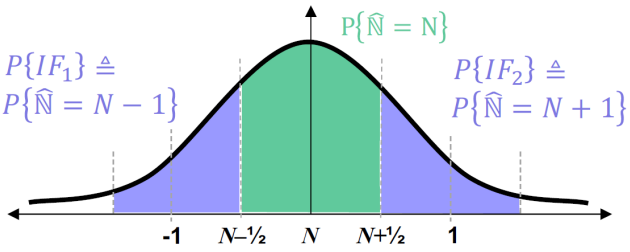

Fig. 2. Example of cycle ambiguity correct and incorrect fix regions

Figure 2 highlights the regions corresponding to a correct fix and incorrect fixes of ± 1 integer cycle.

IV. Monitor False Alarm and Missed Detection

It is practically not possible to integrate the mixed Gaussian distribution in Figure (1) to evaluate the false alarm probability. Given that the correct fix and all incorrect fix events are mutually exclusive and exhaustive events and using the total a law of probability, we may express the false alarm probability under the null hypothesis H0 (fault-free) as

$$P_{fa} = P\{q > T \mid H_0\} = P\{q > T \mid H_0, CF\}P\{CF\} + P\{q > T \mid H_0, IF\}P\{IF\} \quad (20)$$

For simplicity, at this stage, we will conservatively assume that any incorrect fix event will result in a false alarm ($P\{q > T \mid H_0, IF\} = 1$). Since IF and CF events are mutually exclusive and exhaustive, $P\{IF\} = 1 - P\{CF\}$. As a result, the probability of false alarm in (20) can be bounded as

$$P_{fa} \leq P\{q > T \mid H_0, CF\}P\{CF\} + (1 - P\{CF\}) \quad (21)$$

Equation (21) illustrates that the probability of correct fix must be high enough such that the term $(1 - P\{CF\})$ is smaller then the allocated false alarm probability (in the order of 10^{-8} for GBAS CAT III). In order to achieve such probability, the float ambiguity estimate in (13) and (18) needs to be filtered for more than 3 hours, which is not practical. Instead, we will provide a tighter bound on the false alarm probability in (21) by accounting for the impact of some incorrect fixes on the

test statistic, while bounding the effect of the other incorrect fixes [16], [17].

Incorrect fix events in (20) include infinite number of the mutually exclusive discrete incorrect fix events, and when expanded we can rewrite (20) as

$$\begin{aligned} P_{fa} =& P\{q > T \mid H_0, CF\}P\{CF\}+ \\ & \sum_{i=1}^{\inf} P\{q > T \mid H_0, IF_i\}P\{IF_i\} \end{aligned} \tag{22}$$

Now, we will use the same bound technique as in (21), but only for a subset of incorrect fixes (n+1):inf [17].

$$\begin{aligned} P_{fa} \leq& P\{q > T \mid H_0, CF\}P\{CF\}+ \\ & \sum_{i=1}^{n} P\{q > T \mid H_0, IF_i\}P\{IF_i\}+ \\ & (1 - P\{CF\} - \sum_{i=1}^{n} P\{IF_i\}) \end{aligned} \tag{23}$$

Even if many terms are computed in the series term in (23) to provide a tight bound, we may still need to filter for prolonged periods before meeting the required level of P_{fa}. In response, we will introduce multiple threshold regions as illustrated in Figure 2. If the test statistic lies inside the regions corresponding to the correct fix, or the regions corresponding to ± 1 cycle ambiguity, no alarm is triggered. Equation (24) provides a mathematical definition of the threshold regions

$$\{|q| \succ T\} \triangleq \{T < |q| < \lambda - T\} \cup \{|q| > \lambda + T\} \tag{24}$$

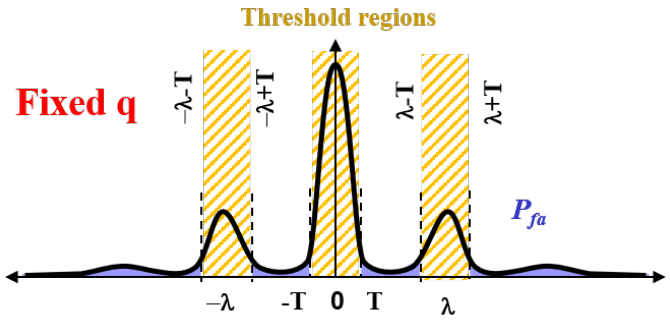

Fig. 3. Illustration of the threshold regions defined in (24)

Using the definition in (24), we may rewrite P_{fa} in (23) as

$$\begin{aligned} P_{fa} \leq& P\{q \succ T \mid H_0, CF\}P\{CF\}+ \\ & \sum_{i=1}^{n} P\{q \succ T \mid H_0, IF_i\}P\{IF_i\}+ \\ & (1 - P\{CF\} - \sum_{i=1}^{n} P\{IF_i\}) \end{aligned} \tag{25}$$

Now, A missed detection will occur if the test statistic is inside the threshold regions under the fault hypothesis H_f (Figure 3)

$$\begin{aligned} P_{md} \leq& P\{q \prec T \mid H_f, CF\}P\{CF\}+ \\ & \sum_{i=1}^{n} P\{q \prec T \mid H_f, IF_i\}P\{IF_i\}+ \\ & (1 - P\{CF\} - \sum_{i=1}^{n} P\{IF_i\}) \end{aligned} \tag{26}$$

V. Monitor Requirements

The probability of false alarm is set to 10^{-8} for both ephemeris monitor and IGM to satisfy the GBAS continuity requirement.

A. Ephemeris monitor

In GBAS Approach Service Type D (GAST-D) CAT III, the current Standards and Recommended Practices (SARPs) has no requirements specifically placed on the ephemeris monitor. Two requirements apply to the post-monitoring error in the corrected pseudorange, and are depicted in Figures 4 and 5 [18]. In both cases, the requirement applies to the probability of missed detection as a function of the size of the error due to the fault. The difference between the two requirements is whether or not there is a prior probability of a fault. Figure 4 represents the requirement without taking the fault prior probability into account. Figure 5 shows the PMD requirements weighted by the prior probability. So, the difference is that in Figure 5, the PMD requirement from the monitor is weighted by the prior probability then sketched and compared to the highlighted area. The ephemeris monitor PMD should satisfy both requirements. In this work, we assume a prior probability of ephemeris fault of 10^{-5}.

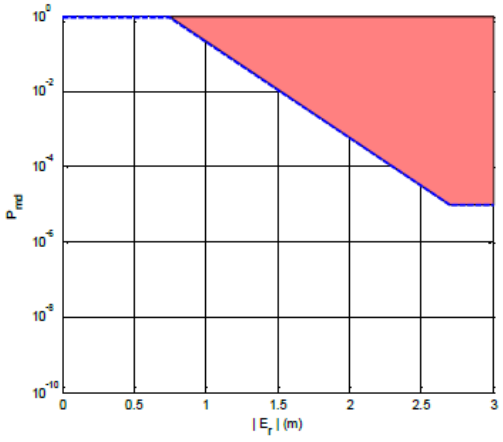

Fig. 4. Requirement on probability of missed detection assuming no a priori knowledge of the probability of a fault.

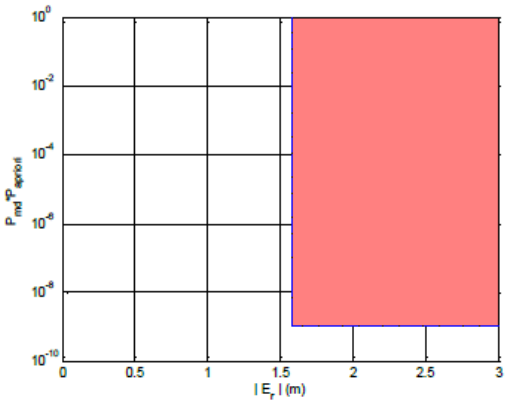

Fig. 5. Requirement on probability of missed detection when a priori knowledge of the probability of a fault is available.

B. IGM

In GBAS Approach Service Type D (GAST-D) CAT III, the integrity risk for IGM is 10^{-9} with an assumed prior probability of ionospheric faults of 10^{-3}. Thus, IGM needs to meet a missed detection probability of 10^{-6}.

Based on experimental analysis of data collected by the Federal Aviation Administration (FAA) Technical Center, it was shown in [19] that the cumulative probability distribution of the double difference carrier phase measurement error can be overbounded by a zero-mean Gaussian distribution with a standard deviation of 6 mm, and the double difference pseudorange is bounded by a standard deviation of 84cm. Based on the same data analysis, the time constant of the pseudorange is 2 sec [19].

In computing the ambiguities for the ephemeris monitor, differential ionospheric error standard deviation of 2mm/km is assumed based on the results in [20], which is converted to a conservative range error using the obliquity factor for a satellite at 3 degree elevation.

VI. Performance evaluation using single baseline.

There are two parameters that drive the performance of the monitor: filtering period and baseline length.

A. Filtering period

Filtering is applied initially to get the ambiguities needed to compute the test statistics. Therefore, the longer the filtering period, the higher the probability of correct ambiguity fix and the longer the monitor has to wait to compute a test statistic and starts monitoring for ephemeris and IGM faults. During this time, GBAS ground will not broadcast the monitored satellite corrections until it is validated by both monitors. Using Equation (21) and the error models described earlier, the ambiguities need to be filtered for 3 hours until the term (1-$P\{CF\}$) is small enough to satisfy the probability of false alarm requirement. Therefore, in the forthcoming analysis, we will use the three threshold region introduced in section (IV).

In the ephemeris monitor, we assume that the reference satellite, which has been validated and tracked for far longer than the tested one, was filtered for 5400 seconds. Based on the false alarm analysis, we needed a filtering period of 605 sec and a threshold of 38mm was adequate to meet 10^{-8} (P_{fa}) using 1000m long baseline. To evaluate P_{md}, different ephemeris fault gradients have been simulated to evaluate P_{md}. For a 3° glide slope, the distance between the aircraft and reference antennas is 5km at the decision height. Therefore, the ranging error resulting from an ephemeris fault is computed by multiplying the ephemeris fault gradient by 5km distance. This process is then repeated for all tested gradient values. Figure (6) shows the resultant P_{md}, where the highlighted area illustrates the ephemeris monitor requirements shown in (4) and (5). The pink diamond points represent probability of missed detection conditioned on a correct fix and weighted by the probability of correct cycle ambiguity(first term in (26)). The green square and blue circle curves represent the terms in (26) corresponding to +1 and -1 incorrect fix respectively. The summation of all three curves (represented by the red curve) shows the total probability of missed detection, which does not satisfy the requirements.

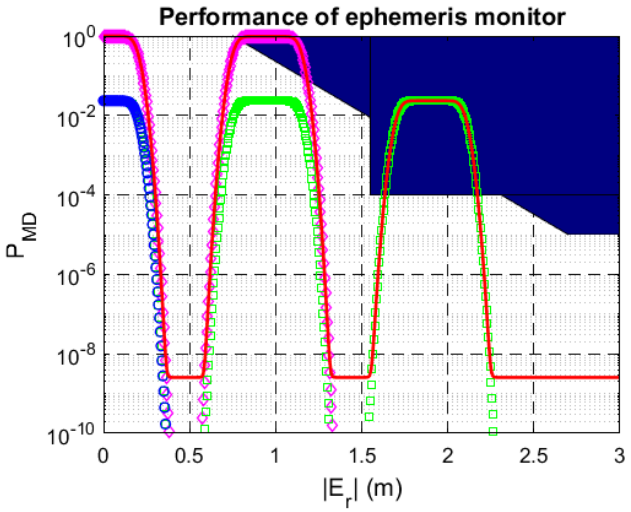

Fig. 6. Pmd vs ranging error using $\pm$ 1 incorrect ambiguity knowledge for 1km baseline.

As for the IGM monitor, a filtering period of 1138 sec and a threshold of 40mm were adequate to satisfy probability of false alarm requirement using 1000m long baseline. Different ionospheric gradients have been simulated to evaluate P_{md}. The continuous horizontal blue line indicates the required the probability of missed detection for IGM. As explained in figure(6), pink diamond, green square and a blue circle (Figure 7) represent three terms of (26) corresponding to the correct cycle ambiguity, -1 incorrect ambiguity and 1 incorrect ambiguity respectively. And, the red curve shows the resultant P_{md} for IGM which illustrates that requirement to detect

ionospheric gradient greater than 300 mm/km is not satisfied.

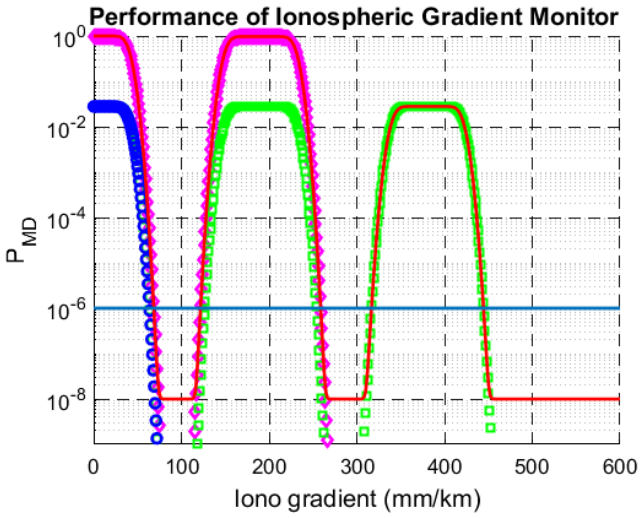

Fig. 7. Pmd vs iono fault gradient using $\pm$ 1 incorrect ambiguity knowledge for 1km baseline.

In both monitors, a further increase in filtering period increases the probability of correct ambiguity fix, while reducing the incorrect fix probability. For the ephemeris monitor, this increase in the filtering period reduces the probability levels in the third peak of the green curve in Figure (6) (helpful in meeting the requirements). However, it will have no effect on reducing the probability levels of the second peak, which corresponding to the correct fix probability (pink curve). Therefore, even if much longer filtering periods are used, the resultant P_{md} will not meet the requirements. This is a byproduct of the introduction of the three threshold regions in Figure (3) needed to meet the false alarm requirement. In contrast, if the 2 hour filtering period is used for the IGM, the third peak in Figure (7) goes below the required value (blue curve), and the second peak does not violate the required value of 300 mm/km, thus meeting the requirement.

B. Baseline length

Now we will investigate the effect of the baseline length on monitor performance. Observing the test statistics in equation (7) and (10), we can see that it is proportional to the baseline length under fault conditions. Thus, increasing the baseline length allow the monitor to detect smaller fault gradients, compared to shorter baselines. For example, the red curve in figures (6) and (7) shifts towards the left. For the ephemeris monitor, figure (8) shows the probability of missed detection for an example baseline length of a 1.5km with filtering period of 656 sec and threshold of 38mm, which meets the requirements. Notice that the filtering period was increased to compensate for the increased differential ionospheric delay that is proportional to the baseline length in (12). Figure (9) shows the probability of missed detection for the same baseline length of 1.5km and filtering period of 1138 sec, which also meets the requirements. Therefore, both monitors meet the requirements if the baseline is at least 1.5km with filtering period of 656 sec for the ephemeris monitor and 1138 sec for the IGM monitor.

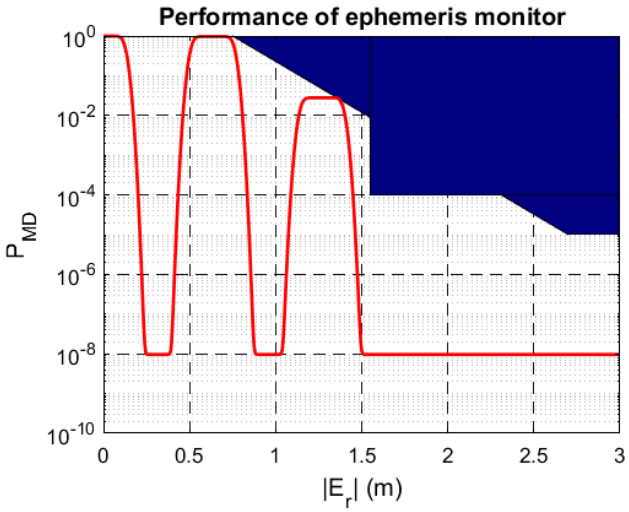

Fig. 8. Pmd vs ranging error using $\pm$ 1 incorrect ambiguity knowledge for a 1.5km baseline.

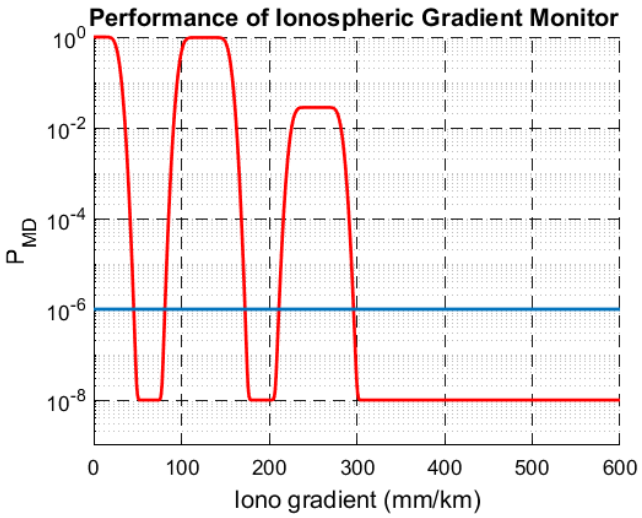

Fig. 9. Pmd vs iono fault gradient using $\pm$ 1 incorrect ambiguity knowledge for 1.5km baseline.

VII. Performance evaluation using Multiple baseline.

In the previous section, we discussed the sensitivity of the monitor's performance to baseline length and filtering periods. But certain airport facilities may have space restriction that does not allow for antennas to be installed 1.5km apart. In this case, we may utilize a second baseline improve the detection performance (figure 10)). In this configuration, the monitor will compute two different test statistics (one for each baseline length) and trigger an alarm if either test statistics exceeds the threshold regions.

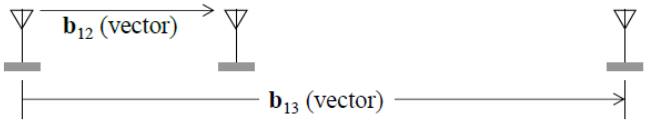

Fig. 10. Illustration of two baselines used for detection

For ephemeris monitor, the test statistics are defined as,

$$\begin{aligned} q_1 &= \Delta^2\phi_{12} - \Delta e^T b_{12} - \lambda(\Delta n_{12}^i - \Delta n_{12}^j) = b_{12}^T \delta e_i + \Delta\nu_{\phi_{12}} \\ q_2 &= \Delta^2\phi_{13} - \Delta e^T b_{13} - \lambda(\Delta n_{13}^i - \Delta n_{13}^j) = b_{13}^T \delta e_i + \Delta\nu_{\phi_{13}} \\ &\text{if} \quad \{q_1 \succ T\} \cup \{q_2 \succ T\} \quad \rightarrow \quad \text{alarm} \end{aligned} \tag{27}$$

And for the IGM monitor, the test statistics are defined as,

$$\begin{aligned} q_1 &= \Delta^2\phi_{12} - \Delta e^T b_{12} - \lambda\Delta^2 n_{12}^{ij} = b_{12}^T \alpha + \Delta\nu_{\phi_{12}} \\ q_2 &= \Delta^2\phi_{13} - \Delta e^T b_{13} - \lambda\Delta^2 n_{13}^{ij} = b_{13}^T \alpha + \Delta\nu_{\phi_{13}} \\ &\text{if} \quad \{q_1 \succ T\} \cup \{q_2 \succ T\} \quad \rightarrow \quad \text{alarm} \end{aligned} \tag{28}$$

Due to using the same antenna in both statistics, q_1 and q_2 will be correlated. The correlation can be captured in the measurement noise covariance matrix. The monitor's test statistics become multidimensional mixed Gaussian distribution. Figure 11 illustrates a probability contour plot of the distribution and the threshold regions of such a monitor. The false alarm probability corresponds to the integration of the distribution over the non-highlighted regions. Mathematically, (25) becomes:

$$\begin{aligned} P_{fa} = P\{q_1 \succ T \cup q_2 \succ T \mid H_0\} = P\{q_1 \succ T \mid H_0\} \\ + P\{q_2 \succ T \mid H_0\} - P\{q_1 \succ T \cap q_2 \succ T \mid H_0\} \end{aligned} \tag{29}$$

Bounding the first two-term in (29) can be carried out as shown in (25). The third term in (29) can be bounded as,

$$\begin{aligned} P\{q_1 \succ \cap\, q_2 \succ T\} \leq P\{q_1 \succ T \cap q_2 \succ T \mid CF_{1\cap 2}\} \\ P\{CF_{1\cap 2}\} + \sum_{k=1}^{l} P\{q_{1k} \succ T \cap q_{2k} \succ T \mid IF_k\} \\ P\{IF_k\} + (1 - P\{CF_{1\cap 2}\} - \sum_{k=1}^{l} P\{IF_k\}) \end{aligned} \tag{30}$$

On the other hand, a missed detection will occur if both test statistics are inside of the threshold regions under the fault hypothesis H_f (Figure 12).

$$P_{md} = P\{q_1 \prec T \cap q_2 \prec T | H_f\} \tag{31}$$

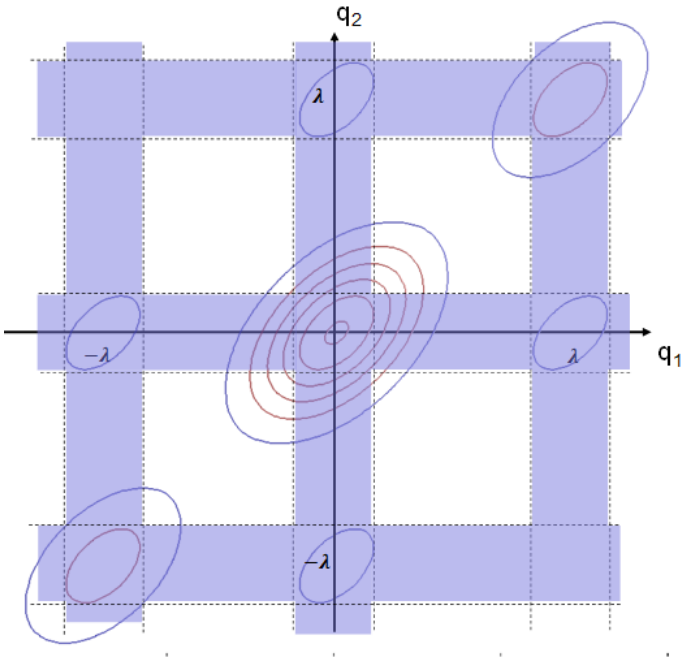

Fig. 11. Contour plot showing the multivariate mixed Gaussian distribution corresponding to the multi-baseline monitor and the threshold regions

Similar to the false alarm probability in the previous subsection, (31) can be bounded as,

$$\begin{aligned} P\{q_1 \prec T \cap q_2 \prec T\} \leq P\{q_1 \prec T \cap q_2 \prec T \mid CF_{1\cap 2}\} \\ P\{CF_{1\cap 2}\} + \sum_{k=1}^{l} P\{q_{1k} \prec T \cap q_{2k} \prec T \mid IFk\} \\ P\{IF_k\} + (1 - P\{CF_{1\cap 2} - \sum_{k=1}^{l} P\{IF_k\}) \end{aligned} \tag{32}$$

Under fault conditions, the mean (which corresponds to the maximum peak of the distribution) of the multivariate mixed Gaussian distribution will be moving along the fault slope as shown in Figure 12. It can be easily shown from (27) that the fault slope, which is the ratio of $\frac{q_2}{q_1}$, is equal to $\frac{b_{13}}{b_{12}}$.

Next, we will investigate the performance of the monitors for two baselines of 200m and 700m long. For the ephemeris monitor, filtering period of 492 sec and threshold of 37mm is adequate to meet the probability of false alarm. Figure 13 shows the resultant P_{md} of the multiple baseline monitor. Unlike Figure 6, where there were three peaks with two penetrating through the highlighted threshold region (Figure 3), in the multiple baseline case, different baseline lengths allow the fault slope to avoid the third threshold region and only one peak is observed on both monitors.

For the IGM monitor, 900 sec of filtering period and a threshold of 35.2mm is adequate to meet the probability of false alarm. Similar the ephemeris monitor, only one peak shows up in the P_{md} curve, due to using the two baseline. However, this configuration of baseline and filtering period

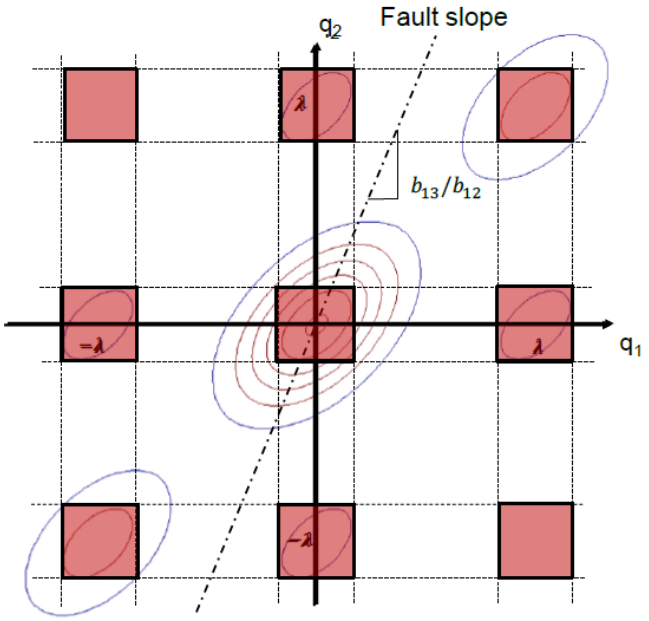

Fig. 12. Contour plot showing the multivariate mixed Gaussian distribution corresponding to the multi-baseline monitor, the missed detection regions, and the fault slope

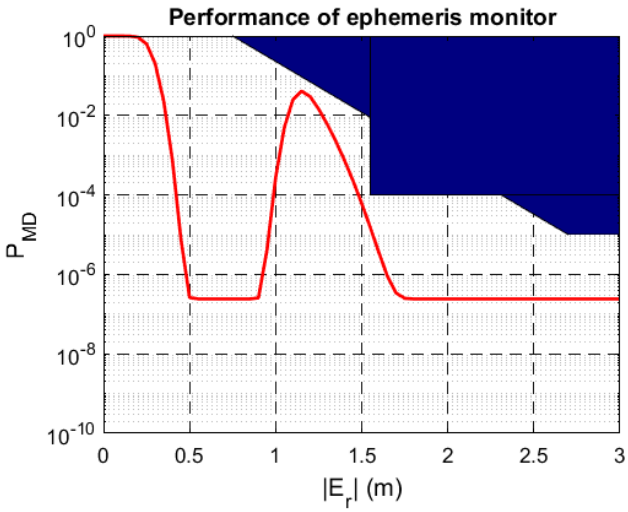

Fig. 13. Pmd vs ranging error using $\pm$ 1 incorrect ambiguity knowledge for 700m and 200m baseline.

only detects gradient greater than 326 mm/km, which exceeds the 300 mm/km requirement. Next, we will investigate couple approaches to improve the IGM performance.

A. Changing baseline length keeping ratio same.

Previously in subsection VI-B, we have seen that increasing the baseline length moves the P_{md} curve towards the left. Therefore, to improve the performance in Figure 14, a longer baseline is expected to shift P_{md} to the left, thus meeting 300 mm/km. For example, we increased the long baseline length to 1km, while keeping the ratio of both baselines the same at 2/7, which results in the 285m baseline. Figure 15 shows that

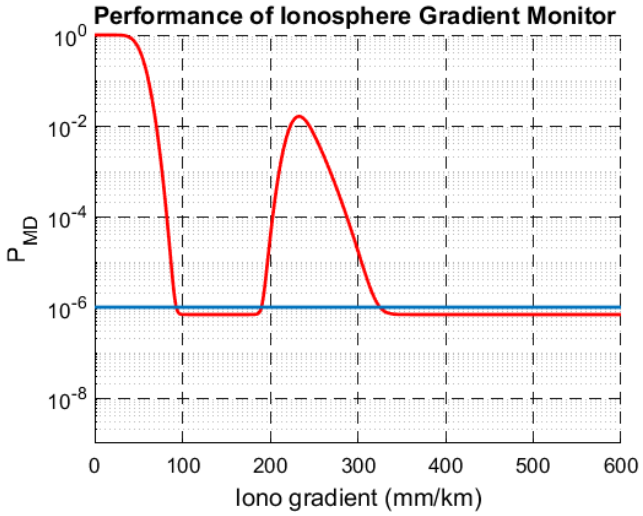

Fig. 14. Pmd vs iono fault gradient using $\pm$ 1 incorrect ambiguity knowledge for 700m and 200m baselines.

the minimum detectable gradient now becomes 225 mm/km, and thus meeting the requirement. This example baseline combination also shifts the P_{md} curve of the ephemeris to the left, thus still meeting the requirement.

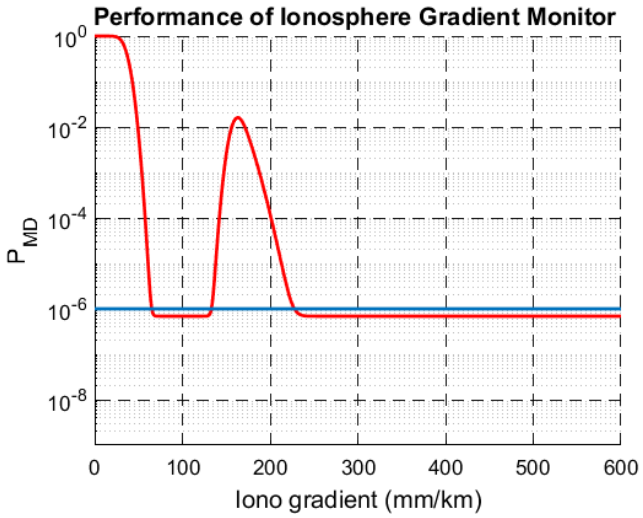

Fig. 15. Pmd vs iono fault gradient using $\pm$ 1 incorrect ambiguity knowledge for 1km and 285m baselines.

B. Modified Threshold regions

In this work, we also considered other methods to improve the monitor performance. For example, 900 seconds of filtering period, during which GBAS ground station is not allowed to broadcast the satellite correction to the aircraft, maybe too long operationally. Therefore, in this section, we consider expanding the threshold regions to include $\pm$2 cycle ambiguities (Figure 17). Equation (33) provides a mathematical definition to Figure 17. We will not implement the 5 threshold region expansion for single the baseline monitor because the

additional regions will generate additional two peaks on figure 9 when the fault passes through the threshold region.

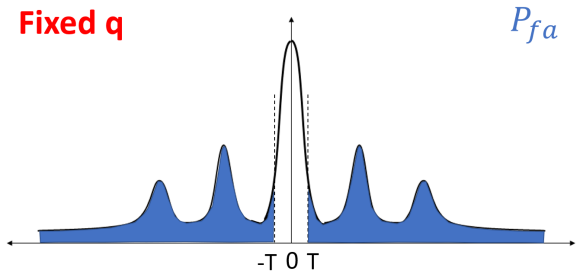

Fig. 16. Illustration of the mixed Gaussian distribution of the test statistic q as a result of rounding $\pm$ 2 cycle ambiguity off.

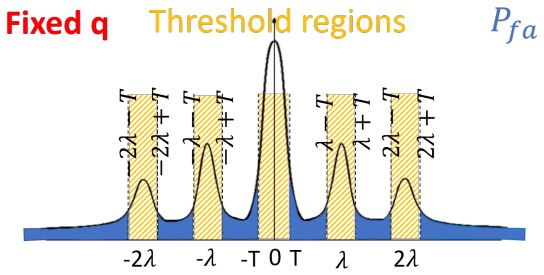

Fig. 17. 5 threshold region for single baseline.

$$\{|q| \gtrless T\} \triangleq \{T < |q| < \lambda - T\} \cup \{\lambda + T < |q| < 2\lambda - T\} \cup \{|q| > 2\lambda + T\} \tag{33}$$

Similarly to Equation (29) and (31), the probability of false alarm and probability of missed detection are expressed in terms of the definition in (33) as shown in (34) and (35).

$$P_{fa} = P\{q_1 \gtrless T \cup q_2 \gtrless T \mid H_0\} = P\{q_1 \gtrless T \mid H_0\} + P\{q_2 \gtrless T \mid H_0\} - P\{q_1 \gtrless T \cap q_2 \gtrless T \mid H_0\} \tag{34}$$

$$P_{md} = P\{q_1 \lessgtr T \cap q_2 \lessgtr T | H_f\} \tag{35}$$

Similar to process explained in sectionVII Equations (34) and (35) can be bounded using equation (25),(30) and(32).

For the IGM monitor, Equation (34) was used in the false alarm analysis where the filtering period that meets the false alarm probability has been reduced to 289 sec with a threshold of 36mm. Using two baseline lengths of 1000m and 285m, the probability of missed detection is plotted in figure 19. As expected, two additional peaks are observed on the P_{md} curve because of the two additional threshold regions. In addition, P_{md} is higher than the requirement of 10^{-6} in this case, because the lowest achieved P_{md} is proportional to $(1-P\{CF\}-\sum P\{IF\})$ as seen in equation (32) (the upper bound for (35)). In this case, increasing the filtering period may help to decreased the lowest P_{md} in Figure 19 but the third and fourth peaks on P_{md} curve are only decreased by 2

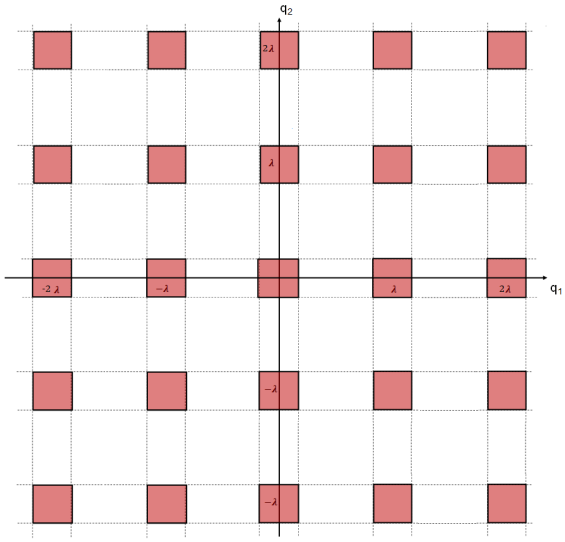

Fig. 18. 25 threshold region for multiple baseline.

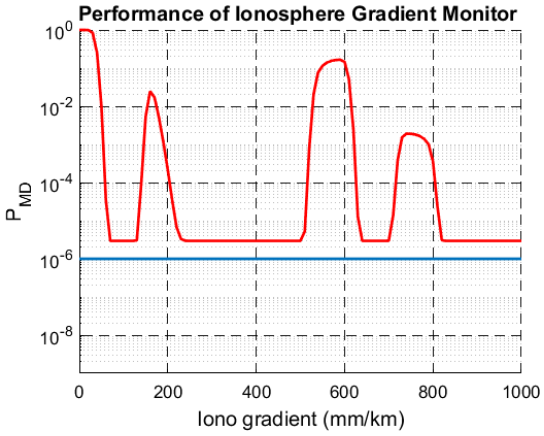

Fig. 19. Pmd vs iono fault gradient using $\pm$ 2 incorrect ambiguity knowledge for 1km and 285m baselines.

hours of filtering. In conclusion, introduction of 5 threshold region is helpful to reduce the probability of false alarm but introduces more peaks on P_{md} curve.

C. Effect of Baseline length ratio

In this subsection, we want to improve the probability of missed detection with the 5 threshold regions. To investigate, Let us start with 1000m and 285m baselines configuration. The fault slope is plotted, in Figure 20, whereas the mean of the fault slides on the fault slope (for different magnitudes), P_{md} increases whenever the fault mean is close to or penetrates the threshold region. Therefore, in Figure 20, the slope penetrates or is close to 4 of the threshold regions (counting the origin of the fault as an example), which explains the four peaks and P_{md} behavior observed in Figure 19. Since the fault slope is proportional to baseline lengths, we can vary the baseline lengths such that the fault slop avoids passing through the threshold regions. By optimization, it is found that baseline

lengths of 1000m and 176m result in the best P_{md} that meets the requirement (Figure 21 and 22). The expansion of the threshold regions can also be applied to the ephemeris monitor. Notice that there is only one optimized baseline lengths ratio (0.176) which satisfies the probability of missed detection for IGM monitor using 5 threshold regions, while few options of baseline length ratio work for the ephemeris monitor. In contrast, using three threshold regions provides wider flexibility in the baseline length ratio (in the range 0.24 to 0.32). The price of this flexibility in baseline lengths using three threshold regions comes at the expense of longer filtering periods as shown in section VII.

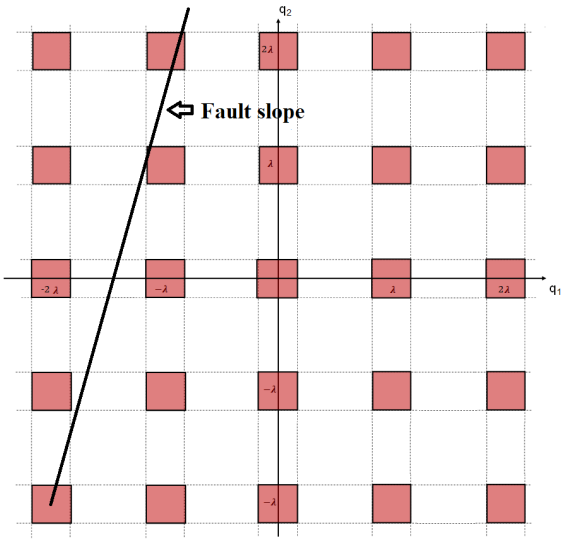

Fig. 20. Worst case fault slope having -2 incorrect ambiguity fixed for baselines 1000m and 285m

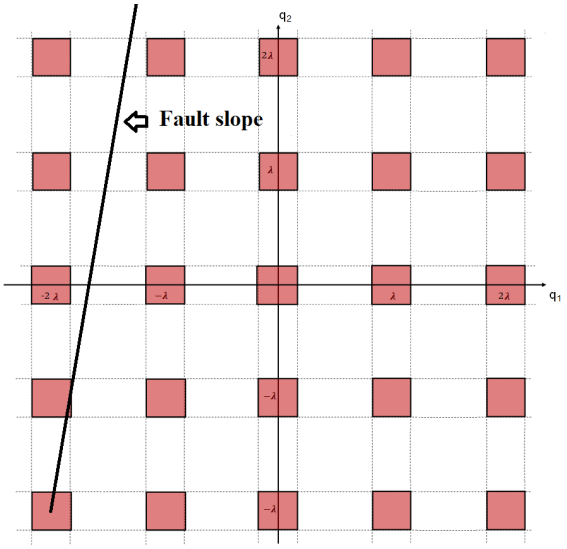

Fig. 21. Worst case fault slope having -2 incorrect ambiguity fixed for baselines 1000m and 176m

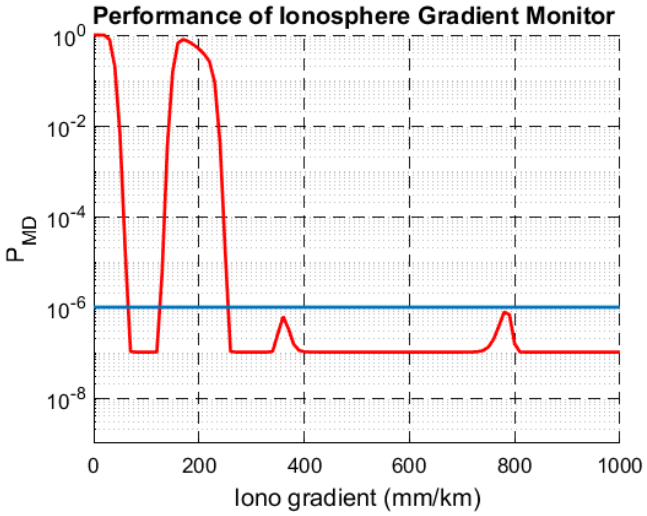

Fig. 22. Pmd vs iono fault gradient using $\pm$ 2 incorrect ambiguity knowledge for 1km and 176m baselines.

VIII. Tropospheric Turbulence

The Spatial gradient monitor developed in section VI and VII are highly sensitive to spatial gradients to satisfy GBAS detection requirements for ionospheric fronts and orbit ephemeris failures detection. However, short duration localized neutral atmospheric disturbances (sometimes called tropospheric turbulence) can also appear as gradients. [21]. Tropospheric turbulence produces small differential measurement errors, which are not hazardous to GBAS users but may still trigger the gradient monitor causing false alarms that will ultimately have an adverse effect on the navigation continuity for GBAS users.

The nominal tropospheric error can be eliminated using differential measurements. However, some localized tropospheric anomalies have been observed [22], [23], which happen due to many reasons: strong wind shears, temperature gradient, unbalanced flow, mountain-waves, and gravity wave wind shear [24]. In [26], tropospheric turbulence caused up to 10cm of double difference carrier phase residual error for a baseline length of about 2.1km. The monitor may interpret the gradient magnitude caused by a tropospheric anomaly to be as large as an ionospheric gradient [21] causing the monitor to trigger an alarm. However, tropospheric anomalies typically exist in the lower atmosphere and only affect small areas. They are no hazardous to aircraft using GBAS because the resulting differential ranging errors are typically on the order of a few centimeters [25].

Since tropospheric turbulence is a local effect, we are proposing to use a parallel replica baseline configuration, but at a distance larger than the scale of tropospheric anomalies. For example, for the multiple baseline configuration in Figure 10, we propose a configuration as shown in Figure 23 to eliminate false alarms by the tropospheric anomalies. An illustrative example, in section VII, the monitor's performance is evaluated for baselines of 1000m and 300m for IGM monitor

(Figure 15). In this case, the monitor will alarm only if both duplicate baselines false alarm (36).

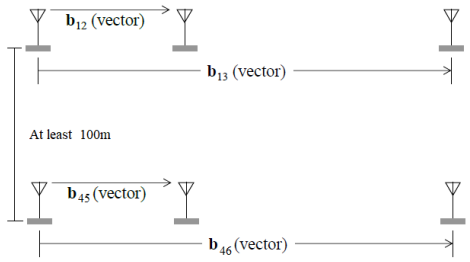

Fig. 23. Illustration of additional baseline under tropospheric turbulence.

$$
\begin{aligned}
q_1 &= \Delta^2\phi_{12} - \Delta e^T b_{12} - \lambda\Delta^2 n_{12}^{ij} = b_{12}^T\alpha + \Delta\nu_{\phi_{12}} \\
q_2 &= \Delta^2\phi_{13} - \Delta e^T b_{13} - \lambda\Delta^2 n_{13}^{ij} = b_{13}^T\alpha + \Delta\nu_{\phi_{13}} \\
q_3 &= \Delta^2\phi_{45} - \Delta e^T b_{45} - \lambda\Delta^2 n_{45}^{ij} = b_{45}^T\alpha + \Delta\nu_{\phi_{45}} \\
q_4 &= \Delta^2\phi_{46} - \Delta e^T b_{46} - \lambda\Delta^2 n_{46}^{ij} = b_{46}^T\alpha + \Delta\nu_{\phi_{46}} \\
&\text{if} \Big\{ \{q_1 \succ T\} \cup \{q_2 \succ T\} \Big\} \cap \Big\{ \{q_3 \succ T\} \cup \{q_4 \succ T\} \Big\} \\
&\rightarrow alarm
\end{aligned}
\tag{36}
$$

Notice that tropospheric turbulence does not impact the cycle resolution for the ephemeris monitor, because it is eliminated in the difference between carrier and code phase measurements (Equation 11). This, however, is not the case when computing code-plus-carrier needed to resolve the ambiguity for the IGM (Equation 15). In order to account for tropospheric error in ephemeris monitor's cycle resolution, FAA data analysis that included those incidents showed that the differential error standard deviation under tropospheric anomalies can be bounded by 14mm. This 14mm was used in computing the standard deviation post filtering ambiguity that was then used in evaluating the probability of fixing in all results shown.

The probability of false alarm and missed detection are given by Equation (37) and (38), respectively, where we assume that as test statistics 1 and 2 are independent of test statistics 3 and 4. The bounds for these probabilities can be derived similarly to Equations (25) and (30). Although the addition of replica baseline configuration will reduce the false alarm probability, because the tropospheric turbulence is local and will impact one of the two configurations, this change has an impact on the probability of missed detection as illustrated in equation (38). Comparing (38) to (31), one can notice that (38) will result in a larger P_{md} than (31) due to the additional statistics from the other configuration, that may have misdetection.

$$
\begin{aligned}
P_{fa} &= P\{\{q_1 \succ T \cup q_2 \succ T\} \cap \{q_3 \succ T \cup q_4 \succ T\} \mid H_0\} \\
&= P\{q_1 \succ T \cup q_2 \succ T \mid H_0\} P\{q_3 \succ T \cup q_4 \succ T \mid H_0\}
\end{aligned}
\tag{37}
$$

$$
\begin{aligned}
P_{md} &= P\{\{q_1 \prec T \cap q_2 \prec T\} \cup \{q_3 \prec T \cap q_4 \prec T\} \mid H_f\} \\
&= P\{q_1 \prec T \cup q_2 \prec T \mid H_f\} + P\{q_3 \prec T \cup q_4 \prec T \mid H_f\} \\
&\quad - P\{q_1 \prec T \cup q_2 \prec T \mid H_f\} P\{q_3 \prec T \cup q_4 \prec T \mid H_f\}
\end{aligned}
\tag{38}
$$

From (37), it is evident that a filtering period of 900 sec as in section VII is sufficient to meet P_{fa} requirement for baseline lengths of 1km and 285m. However, the additional terms in P_{md} will cause the low probability flat portion of P_{md} to be greater than the requirement. Therefore, 1100 sec filtering period is required to satisfy the probability of missed detection requirement (Figure 24). The same baseline configuration with 600 sec filtering period was sufficient to meet the ephemeris monitor requirement as shown in Figure 25.

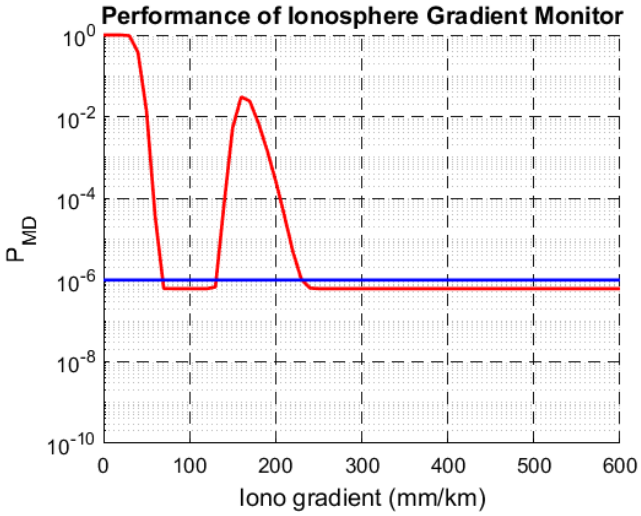

Fig. 24. Pmd vs iono fault gradient under tropospheric turbulence using $\pm$ 1 incorrect ambiguity fix for 1km and 285m baselines.

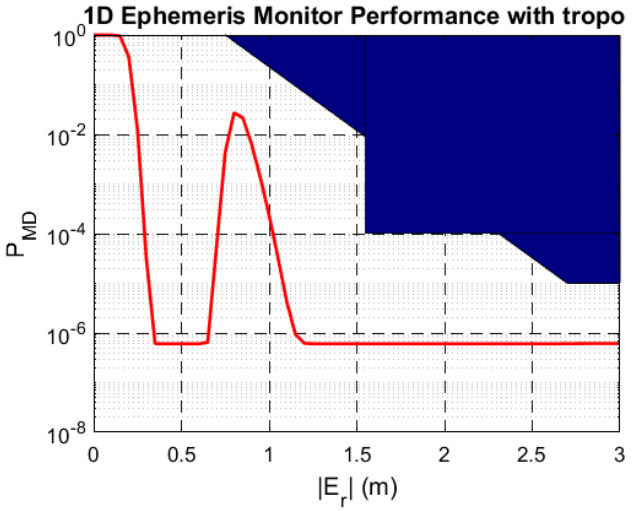

Fig. 25. Pmd vs ranging error under tropospheric turbulence using $\pm$ 1 incorrect ambiguity fix for 1km and 285m baselines.

IX. Conclusion

In this paper, we introduced a new differential carrier phase based monitor that utilizes the pseudorange measurements to resolve the cycle ambiguities and extract the most of the carrier phase sensitivity to detect spatial gradient faults due to its low noise. The likelihood of wrong ambiguity fix is accounted for in evaluating the false alarm and missed detection probabilities. We discussed different parameters that impact the performance of the monitor and the way they affect missed detection and false alarm probabilities. We also address the monitor's performance subject to tropospheric turbulence by adding additional baseline. In the future, we will extend the developed monitor to detect multiple dimensional spatial gradient faults.

Acknowledgment

The authors would like to thank the Federal Aviation Administration (FAA) for their continued support of this research effort. The opinions in this paper are our own and do not represent those of the FAA, any other person or organization.

References

[1] Khanafseh, Samer, Pullen, Sam, Warburton, John, Carrier Phase Ionospheric Gradient Ground Monitor for GBAS with Experimental Validation, NAVIGATION, Vol. 59, No. 1, Spring 2012, pp. 51-60.

[2] Jing, J., Khanafseh, S.K., Chan, F.-C., Langel, S., Pervan, B., "Detecting Ionospheric Gradients for GBAS Using A Null Space Monitor," Proceedings of IEEE/ION PLANS 2012, Myrtle Beach, South Carolina , April 2012, pp. 1125-1133.

[3] Luo, M., Pullen, S., Walter, T., and Enge, P., Ionosphere Spatial Gradient Threat for LAAS: Mitigation and Tolerable Threat Space, Proceedings of the National Technical Meeting of The Institute of Navigation, San Diego, CA, January 2004, pp. 490501.

[4] J. Jing, S. Khanafseh, S. Langel, F-C. Chan, and B. Pervan. "Null Space Ephemeris Monitor for GBAS". Proceedings of the ION 2013 Pacific PNT Meeting. Honolulu, HI. April 2013, pp. 978-985.

[5] Pervan, B., and Chan, F., Detecting Global Positioning Satellite Orbit Errors Using Short-Baseline Carrier Phase Measurements, Journal of Guidance, Control, and Dynamics, Vol. 26, No. 1, Jan.-Feb., 2003

[6] Tang, H., Pullen, S., Enge, P., Gratton, L., Pervan, B., Brenner, M., Scheitlin, J., Kline, P., "Ephemeris Type A Fault Analysis and Mitigation for LAAS," Proceedings of IEEE/ION PLANS 2010, Indian Wells, CA, May 2010, pp. 654-666.

[7] B. Pervan and L. Gratton. Orbit ephemeris monitors for local area differential gps. IEEE Transactions on Aerospace and Electronic Systems, 41.2, 2005.

[8] S. Pullen, Y. S. Park, and P. Enge, "Impact and mitigation of ionospheric anomalies on ground-based augmentation of GNSS," Radio Science, vol. 44, 2009.

[9] T. Murphy and S. Naerlich, "SARPs for GNSS Elements and Signals (GBAS)," in Navigation Systems Panel (NSP) Working Group of the Whole Meeting, (Montreal, Canada), May 2010.

[10] S. Jin, L. Han, and J. Cho, "Lower atmospheric anomalies following the 2008 Wenchuan Earthquake observed by GPS measurements," Journal of Atmospheric and Solar-Terrestrial Physics, vol. 73, May 2011.

[11] A. Mahalov, "3D Dynamics and Turbulence Induced By Mountain and Inertia- Gravity Waves in the Upper Troposphere and Lower Stratosphere (UTLS)," 6th AIAA Theoretical Fluid Mechanics Conference, 2011.

[12] Y. Ahn, D. Kim, and P. Dare, "Local Tropospheric Anomaly Effects on GPS RTK Performance," in Proceedings of the 19th International Technical Meeting of the Satellite Division of The Institute of Navigation, 2006.

[13] Jing, Jing, Khanafseh, Samer, Langel, Steven, Pervan, Boris, "Detection and Isolation of Ionospheric Fronts for GBAS," Proceedings of the 27th International Technical Meeting of The Satellite Division of the Institute of Navigation (ION GNSS+ 2014), Tampa, Florida, September 2014, pp. 3526-3531.

[14] Khanafseh, Samer M. et al. "Carrier Phase Ionospheric Gradient Ground Monitor for GBAS with Experimental Validation." Proceedings of the 23rd International Technical Meeting of the Satellite Division of the Institute of Navigation (ION GNSS-2010), Portland, OR, September 21-24, 2010.

[15] Ming Luo "LAAS Study of Slow-Moving Ionosphere Anomalies and Their Potential Impacts. " ION GNSS 18th International Technical Meeting of the Satellite Division, 13-16 September 2005, Long Beach, CA

[16] S. Khanafseh and S. Langel, Implementation and Experimental Validation of Cycle Ambiguity Resolution with Position Domain Integrity Risk Constraints, NAVIGATION: Journal of the Institute of Navigation, Vol. 58, No. 1, Spring 2011, pp. 45-58.

[17] Samer Khanafseh and Boris Pervan, A New Approach for Calculating Position Domain Integrity Risk for Cycle Resolution in Carrier Phase Navigation Systems, IEEE Transaction on Aerospace and Electronic Systems, Vol. 46, No. 1, Jan. 2010

[18] Tim Murphy,Stefan Naerlich, "SARPs for GNSS Elements and Signals (GBAS),"Navigation Systems Panel (NSP) Working Group of the Whole Meeting, Montreal, 17 28 May 2010

[19] Khanafseh, S., Patel, J., and Pervan B., Ephemeris Monitor for GBAS using multiple baseline antennas with experimental validation, Proceedings of the 30th International Technical Meeting of The Satellite Division of the Institute of Navigation (ION GNSS+ 2017), Portland, Oregon, September 2017.

[20] Lee, J., Pullen, S., Datta-Barua, S., and Enge, P., Assessment of Ionosphere Spatial Decorrelation for Global Positioning System-Based Aircraft Landing Systems, Journal of Aircraft, Vol. 44, No. 5, 2007, pp. 16621669

[21] K. Alexander, "Observed Nominal Atmospheric Behavior Using Honeywell's GAST D Ionosphere Gradient Monitor," in Navigation Systems Panel (NSP) CAT II/III Subgroup (CSG), (Montreal, Canada), May 2014.

[22] J. Y. N. Cho and R. E. Newell, "Characterizations of tropospheric turbulence and stability layers from aircraft observations," Journal of Geophysical Research, vol. 108, no. D20, 2003.

[23] S. Jin, L. Han, and J. Cho, "Lower atmospheric anomalies following the 2008 Wenchuan Earthquake observed by GPS measurements," Journal of Atmospheric and Solar-Terrestrial Physics, vol. 73, May 2011.

[24] R. D. Sharman, S. B. Trier, T. P. Lane, and J. D. Doyle, Sources and dynam- ics of turbulence in the upper troposphere and lower stratosphere: A review," Geophysical Research Letters, 2012.

[25] F. van Graas and Z. Zhu, "Tropospheric Delay Threats for the Ground Based Augmentation System," in Proceedings of the 2011 International Technical Meet- ing of The Institute of Navigation, 2011.

[26] Y. Ahn, D. Kim, and P. Dare, "Local Tropospheric Anomaly Effects on GPS RTK Performance," in Proceedings of the 19th International Technical Meeting of the Satellite Division of The Institute of Navigation, 2006.